Statistical mechanics of magnetic bubble arrays. I. Topology and thermalization

R. Seshadri and R. M. Westervelt
Division of Applied Sciences and Department of Physics, Harvard University, Cambridge, Massachusetts 02138
(Received 5 March 1992)

Bubble domains in thin magnetic garnet films are an experimentally accessible two-dimensional system with well-characterized properties. Bubble arrays can be directly viewed with polarized light using optical microscopy, digital imaging, and computer-video techniques. The structure and dynamics of topological defects can be studied in detail. We present observations of the interactions and dynamics of defects in magnetic bubble arrays. Quasithermal Brownian motion of bubbles in an applied ac magnetic field arises from microscopic substrate roughness. Experimental measurements of diffusive bubble motion are used to estimate the effective temperature, and the effective pinning energy and length scales for microscopic roughness in the garnet film.

I. INTRODUCTION

Two-dimensional systems have generated considerable interest in modern statistical mechanics and condensed matter physics. Theoretical studies on two-dimensional systems have focused on the characteristics of order and on the nature of the transition from order to disorder.[1–3] Two-dimensional systems lie between three-dimensional systems that can be ordered at finite temperatures and one-dimensional systems that are always disordered. Topological defects play an important role in the transition from order to disorder, which has been addressed in theory.[1–3]

Two-dimensional systems are attractive for experimental measurements, and have been investigated for some time. Systems of hard spheres,[4] polystyrene colloids,[5–8] magnetic holes in ferrofluids,[9] vortex arrays in high-temperature superconductors,[10,11] liquid crystals,[2] electrons on Helium,[2] and noble gases physisorbed on substrates[2] have been studied. In many of these experimental systems (with the notable exceptions of colloids and ferrofluids) the microscopic structural details are not accessible. In these cases direct observations are not experimentally feasible using existing techniques, and only macroscopic properties are measured.

Magnetic garnet films are a highly developed material system.[12–14] These garnet films display a rich variety of domain structures with ordered phases and order-disorder transitions. Of the different types of domains that can be nucleated in these garnet films magnetic bubble domains are the best characterized.[15–20] The motion of magnetic bubbles can be directly observed and followed in time. Arrays of bubbles form an interesting and novel system in which to study the statistical mechanics of two-dimensional systems. The order-disorder transition in two-dimensions can be studied in detail, because the topological defects can be visualized and the microscopic structural details are directly accessible. Assumptions concerning microscopic structure made in theory can be directly tested and verified. In these experiments thermal motion is simulated by the application of an ac magnetic field. The ac field induces a slight breathing motion of a bubble, produced by a small periodic contraction and expansion of the bubble radius. Microscopic roughness in the garnet couples to this motion to produce a jitter in the location of the bubble. Because the force due to roughness has different values at different points, the jitter of each bubble is spatially and temporally uncorrelated with the jitter of other bubbles in the lattice-simulating thermal motion. Magnetic garnet films also show other domain patterns including cellular domains that exhibits a topological coarsening process analogous to soap froths and ordered honeycomb cellular structures that undergo a sharp topological transition to a disordered froth,[21–25] and strip patterns analogous to Langmuir films that exhibit a topological disordering transition.[26,27]

In this paper we describe the statistical mechanics of two-dimensional arrays of magnetic bubbles in garnet films. We describe observations of different topological defects and the process of thermalization of defects in magnetic-bubble arrays. In part II, a companion paper (see Ref. 29) we describe observations of two-dimensional melting as the density of bubbles in the array is decreased. We begin in Sec. II of this paper (part I) with an introduction to the properties of magnetic bubbles and bubble arrays in our garnet films. In Sec. III we describe the methods used to observe bubbles and structural defects in arrays. In Sec. IV we describe experimental observations of the dynamics of topological defects, which play an important role in the melting transition. In Sec. V we describe the thermal motion of bubbles produced by a superimposed ac magnetic field, and measurements of the effective temperature. In Sec. VI we summarize our conclusions. A brief early account of this work appeared in Ref. 28.

II. BUBBLES AND BUBBLE ARRAYS IN GARNET FILMS

In this section we discuss the basic properties of magnetic bubbles and bubble arrays from a theoretical and an experimental point of view, and describe the characteristics of our samples.

As illustrated in Fig. 1(a), a magnetic bubble is a cylindrical domain of reversed magnetization in a garnet film. We observe magnetic bubble arrays in a bismuth-substituted iron garnet film with material composition $Fe_{3.91}Y_{1.20}Bi_{1.09}Gd_{0.95}Ga_{0.76}Tm_{0.09}O_{12}$ grown by liquid phase epitaxy at the Airtron Division of Litton Industries for use in magneto-optic devices.[30] The film has bulk magnetization $4\pi M = 190$ G, thickness $h = 7.8$ μm, and Curie point $T_{\text{curie}} = 170\,^{\circ}\text{C}$. Like most garnet films developed for devices, this film has strong growth induced uniaxial magnetic anisotropy with easy axis perpendicular to the film plane. The anisotropy supports domains comprised of magnetization aligned with or opposed to a perpendicular applied field H_B. The domain walls are narrow (~ 0.1 μm) compared to the domain sizes (~ 10 μm), and have an effective domain wall energy density (σ_W) of 0.23 ergs/cm^2 measured using known expressions for the demagnetization field of isolated bubbles and stripes.[16] Because bubbles move without substantial deformation in the film via lateral translation of domain walls, bubble motion is essentially two dimensional. The garnet films are grown in ultraclean conditions to minimize microscopic material defects which contribute to coercive friction that inhibits domain motion. Areas of the wafer close to the center are used to avoid nonuniformities that develop near the edges in the growth process. Our sample has a usable low-defect area of 3 cm^2.

The energetics of an isolated bubble domain such as the one shown in Fig. 1(a) have been thoroughly studied for device applications.[12–20] The total energy E_{IB} of an isolated bubble with respect to saturation (all the magnetization aligned perpendicular to the film and bubble absent) is

$$E_{\text{IB}} = E_W + E_H + E_M \ . \tag{1}$$

The wall energy is $E_W = \sigma_W A$, where σ_W is the domain wall energy per unit area and A is the area of the wall.

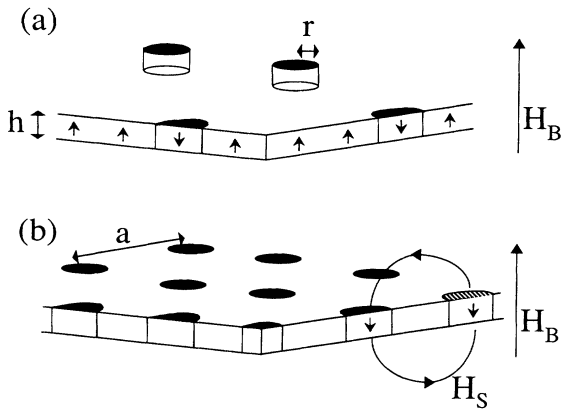

FIG. 1. (a) Schematic diagram of magnetic garnet film (thickness h) with four cylindrical magnetic bubble domains (radius r). Arrows represent film magnetization. A perpendicular dc bias magnetic field H_B is applied opposing the bubble magnetization as indicated. (b) Schematic diagram of hexagonal bubble array (lattice spacing $a > h,r$). Stay fields H_S from neighboring bubbles at the site of the striped bubble add to the bias field H_B, as shown.

The field energy $E_H = \mu H_B$ is the magnetic energy of the bubble's magnetic dipole moment μ in the applied perpendicular magnetic field H_B and E_M is the demagnetization energy. For an isolated bubble measured with respect to saturation, E_M represents a gain in energy due to flux closure between oppositely aligned magnetization on either side of the domain wall. At a given value of the applied field H_B the bubble radius r adjusts to minimize the total energy E_{IB}. There are two physically important values of H_B for isolated bubbles that bound the range of bias fields within which the bubble is stable and energetically favorable. Isolated bubbles collapse at a field $H_B = H_{CO}$, for which the bubble radius r is r_{CO}. Both H_{CO} and r_{CO} are well defined and reproducible values for a particular garnet film. The collapse field H_{CO} places an upperbound on the range of H_B where an isolated bubble domain is stable. A lower bound on the range of stable fields is the run-out field H_{RI}, at which the isolated bubble elongates into a stripe (here RI stands for run-in from stripe to bubble domains).[12,13]

An array of magnetic bubbles is illustrated in Fig. 1(b). Ferromagnetic materials break into many domains in order to reduce the total energy.[31] However, the evolution of the pattern of magnetization is limited by the constraints associated with the creation or destruction of a domain, and typical patterns are metastable. Under the conditions studied here for which only bubble domains are present, the number of bubbles is constant at a given field H_B, and they arrange themselves to reduce the total energy. The total energy E_{array} of an array of bubble domains shown in Fig. 1(b) has two terms

$$E_{\text{array}} = NE_{\text{IB}} + E_{\text{Int}} \ . \tag{2}$$

The first term arises from the energy of isolated bubbles in the applied magnetic field. This equals the product of the number of bubbles present N and the energy of one isolated bubble E_{IB} from Eq. (1). The second term E_{Int} arises from the repulsive interaction between bubbles. As shown in Fig. 1(b), at the site of any bubble the stray field produced by all other bubbles in the film add to the applied bias field H_B. This repulsive pairwise interaction between bubbles is well approximated by a dipole-dipole interaction when the interbubble spacing is larger than the bubble size r and the thickness of the film h.[32] Given a uniform film magnetization M, the dipole moment of the bubbles is $\mu = 2M\pi r^2 h$, where the factor $2M$ is the change in magnetization with respect to saturation. For a fixed number N of bubbles, the bubble array is under pressure as a result of the repulsive forces between bubbles, and the conditions at the boundary of the array are important. The energetically favorable configuration for an array of bubbles far from the boundaries is a triangular lattice.

Bubble arrays were produced from a sea of bubbles, created by first applying and then removing a strong in-plane magnetic field of 2.5 kOe which overcomes the uniaxial anisotropy. This technique is standard, and the properties of the bubble sea are reproducible and uniform throughout the film. This sea of bubbles is initially disordered and has a high density (~ 8000 mm^{-2}). Polycrys-

talline bubble arrays with large crystallite sizes of $\sim 12\,000$ bubbles and bubble densities of ~ 4000 mm^{-2} were produced from the sea by annealing in superimposed spatially uniform ac and dc magnetic fields for a period of 4 h.[33] The amplitude and frequency of the ac field were $H_{ac}=20$ Oe peak-to-peak and $\nu=40$ Hz, and the value of the dc bias field was $H_B=75$ Oe, opposite to the bubble magnetization.

Our experiments were conducted with an adjustable applied bias field H_B oriented to oppose the magnetization of the bubbles. As the bias H_B is increased from zero, the net bubble magnetization which opposes H_B decreases in four regimes. At small values of H_B, the number of bubbles remains constant, and their radii decrease with increasing H_B (regime 1). At sufficiently large values of H_B, the local field at some places in the film exceeds the collapse field H_{CO} and some bubbles are destroyed as H_B increases; at intermediate fields the bubble radii also continue to decrease (regime 2). At larger values of H_B (above 75 Oe for our samples) the bubble radius does not change significantly as the field is increased and is uniform from bubble to bubble. In this regime the net bubble magnetization decreases primarily via the destruction of bubbles as their local field reaches H_{CO} (regime 3). At very large values of H_B the areal density of the bubbles is low and bubble-bubble interactions are negligible (regime 4). We call this the isolated bubble regime. Isolated bubbles collapse when the applied bias field reaches the collapse field $H_B=H_{CO}$, which for our sample is $H_{CO}=103$ Oe in the absence of an ac field.

III. VISUALIZATION OF BUBBLE ARRAYS

We can directly observe this two-dimensional system and follow the bubble motion in time. We use optical microscopy and the Faraday rotation of transmitted polarized light to observe magnetic bubbles. The Airtron garnet film contains a large concentration of bismuth and has an unusually large ratio of magneto-optic rotation to absorption.[30] Thus, images obtained are bright and have high contrast. These images were recorded via a charge-coupled-device camera, a video corrector, and an S-VHS videocassette recorder onto videotape. The videocassette recorder is interfaced to a computer through a frame-grabber board, which was programed to capture video images as a function of time by continuously converting the video signal into bitmaps.

Our measurements are expressed in terms of the motion of the centers of the bubbles in an array. The sequence of image-processing steps used to extract the bubble centers from videodata is illustrated in Figs. 2(a)–2(c). Figure 2(a) shows a section of a typical grey scale recorded image. Grey scale images were digitally processed to equalize intensity differences across the field of view, and then thredholded to produce sharp black and white pictures as shown in Fig. 2(b). This technique accurately locates $\sim 98\%$ of the bubbles in the image. The errors in locating the few remaining bubbles were usually due to dust particles on the sample or in the optics. The bubbles in these areas were carefully isolated by hand after identifying the dust on the grey scale image. The algorithm used for intensity equalization consists of dividing the picture into squares of a specific size (20 pixels$\times$20 pixels), and then subtracting the average grey scale value of each square from each pixel in that square. Our measurements indicate that this algorithm does not introduce significant distortions in the array of bubble centers.

After thresholding, the location of each bubble in the picture was computed from the arithmetic means of the x and y coordinates of all the pixels representing each bubble, and the area of each bubble was determined from the sum of the number of pixels. A spatial low-pass filter was used to remove spurious single-pixel noise from the images. The product of these steps is illustrated by Fig. 2(c), which consists of an array of points at the centers of the bubbles in Figs. 2(a) and 2(b). Note that the spatial resolution in Fig. 2(c) is greater than that of either Fig. 2(a) or 2(b); as a result of averaging the uncertainly in the location of bubble centers is less than one pixel in the original image. The area of each recorded image was 1078×808 μm^2 and the number of bubbles in an image was as large as $N\sim 3000$, for which the bubble spacing is ~ 10 pixels (17 μm).

Topological defects in bubble arrays are difficult to determine by eye, especially when the number of defects is large. We used Voronoi constructions to unambiguously determine the type and location of topological defects in arrays of bubble centers such as Fig. 2(c). A Voronoi construction is the cellular pattern formed by the perpendicular bisectors of all line segments joining neighboring bubbles; for each bubble site the correct cell is the smallest polygon formed by any possible combination of perpendicular bisectors. This construction is unique for a given set of points. Topological defects can be expressed in terms of disclinations, which are sites with greater or fewer than six adjacent sites. A site with a five-sided polygon in the Voronoi construction is a fivefold disclination with topological charge -1, and a site with a seven-sided polygon is a sevenfold disclination with topological charge $+1$. This construction also measures the quantities necessary to probe orientational order, specifically the midpoints of the lines connecting adjacent bubbles (bond centers), and the angles these lines make with respect to the horizontal (bond angles). The algorithm used to implement Voronoi constructions is described Ref. 34.

Figure 3(a) is the Voronoi construction for the bubble center array shown in Fig. 2(c). The disclinations identified using the construction in Fig. 3(a) are displayed in Fig. 3(b): here the black squares correspond to fivefold disclinations and the black circles correspond to sevenfold disclinations. A black circle and a black square separated by one lattice spacing corresponds to an edge dislocation.

IV. TOPOLOGICAL DEFECTS IN BUBBLE ARRAYS

In this section we present direct observations and measurements of the properties and interactions of topological defects in bubble arrays. The evolution of bubble arrays and topological defects can be viewed directly in

space and time as described in the previous section. Bubble arrays are a real physical system in which the static and dynamic properties of topological defects can be studied. Early observations of topological defects in closely packed bubble arrays (in regime 1 or 2) were made by Woolhouse and Chaudhari.[33]

In a perfect hexagonal lattice all bubbles are sixfold coordinated and the Voronoi construction is a perfect honeycomb structure. As illustrated in Figs. 4(a) and 4(b), fivefold and sevenfold disclinations can be made from a perfect hexagonal crystal by removing or adding one 60° wedge. As shown, the strain field associated with an isolated disclination is approximately rotationally symmetric and independent of distance from the disclination, and the total strain energy increases with the size of the system.[35,36] In our bubble arrays we observe four-, five-, seven-, and eightfold disclinations. As shown in Fig. 4(a) and 4(b) isolated disclinations destroy both translational and orientational order in a lattice.[1]

Isolated disclinations with opposite topological charge attract each other strongly and form clusters which correspond to more complex topological defects. A five-seven disclination pair forms an edge dislocation, which corresponds to two additional half-rows of bubbles, indicated by the dotted lines in Fig. 4(c). Dislocations do not destroy orientational order, but do destroy translational order, as seen by the Burger's circuit around the dislocation in Fig. 4(c) (heavy black line) which does not close upon itself.[1] In our arrays we commonly observe five-seven edge dislocations, as shown in Fig. 3(b). Dislocations move relatively easily in the glide direction perpendicular to the line joining the five- and sevenfold disclinations, but less easily in the climb direction parallel to this line, because climb involves the absorption and emission of vacancies and interstitials while glide does not. Dislocations produce a dipolar strain field which falls off with distance as $1/r$, and the energy associated with a dislocation increases as the logarithm of the system size.[35,36]

Isolated dislocations attract each other via their strain fields, and form more complex defects composed of two

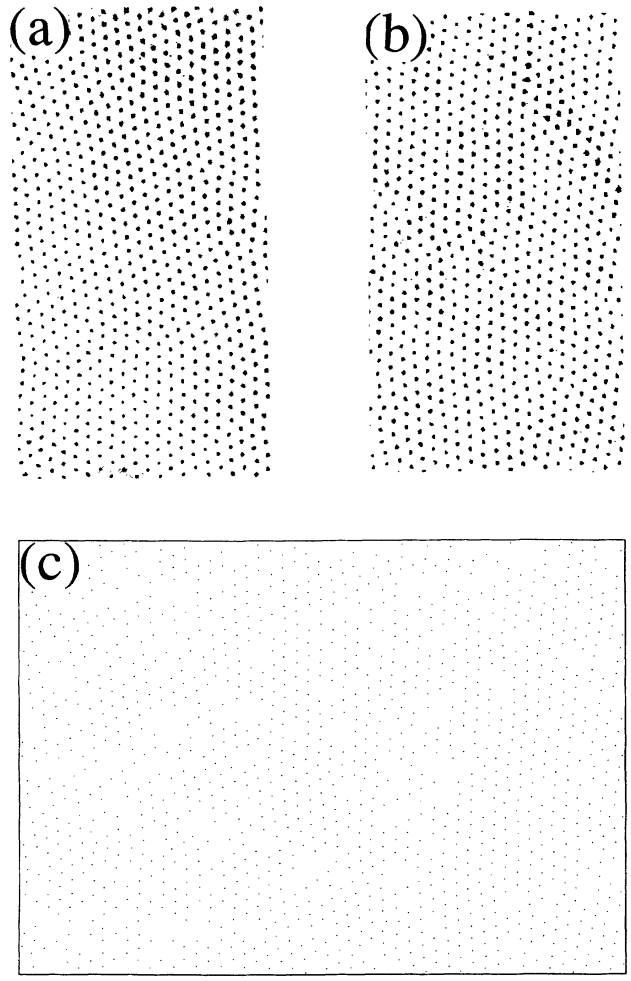

FIG. 2. (a) Section of a grey scale image of a bubble array as acquired. (b) Section of the image after equalizing and thresholding. (c) Bubble locations determined form the thresholded image; dots correspond to the bubble centers.

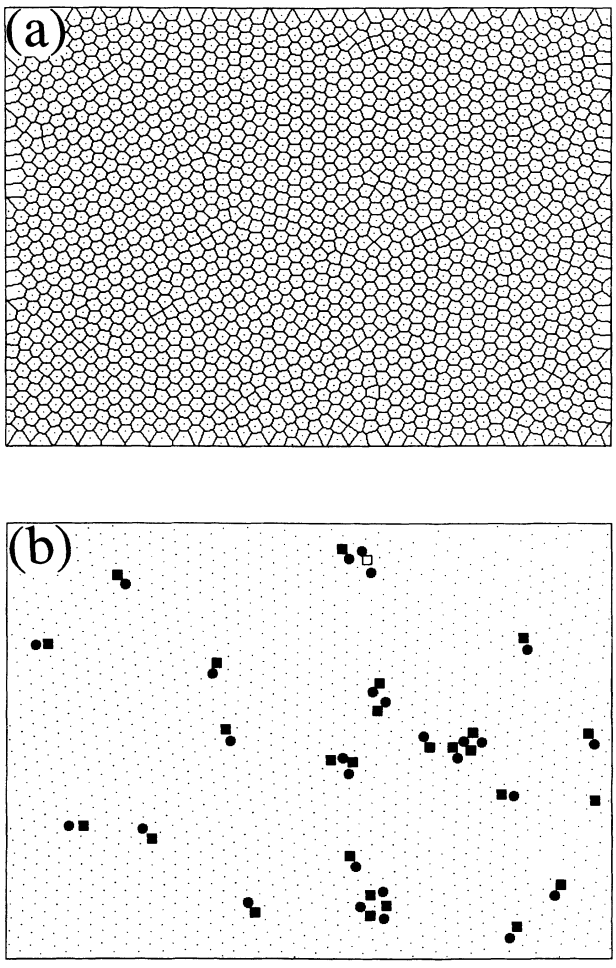

FIG. 3. (a) Voronoi construction of the bubbles center array in Fig. 2(c); this construction is used to determine bond information and isolate lattice defects. (b) Topological defects isolated from the Voronoi construction in (a). The open squares, black square, and black circles correspond to four-, five-, and sevenfold disclinations (see text).

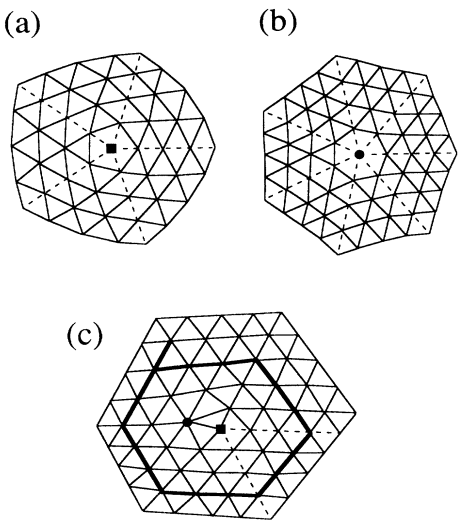

FIG. 4. Topological defects commonly observed in two-dimensional magnetic bubble arrays: (a) and (b) are five- and sevenfold disclinations and (c) is an edge dislocation formed from a five-seven disclination pair. The dashed line in (a) and (b) denote what would be 60° wedges in the corresponding hexagonal lattice without defects. The dashed lines in (c) denote two extra rows in the lattice, associated with the dislocation. The heavy black line in (c) is a Burger's circuit around the dislocation.

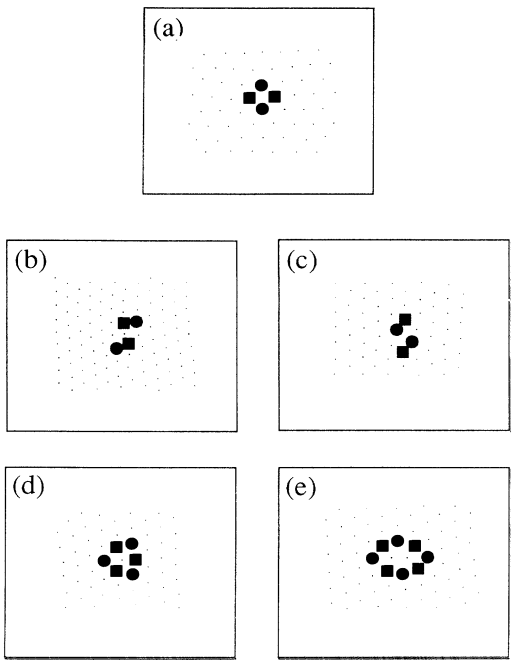

FIG. 5. Sections of bubble array images showing common defect structures with zero net Burger's vector. The dislocation pair in (a) corresponds to a virtual pair, also called a twisted bond or lattice shear. The dislocation pairs in (b) and (c) correspond to an interstitial and a vacancy, respectively. The three- and four-dislocation clusters in (d) and (e) correspond to interstitials and can be obtained from (b) via dislocation glide.

or more dislocations. Examples of different types of defects from bubble array data are shown in Figs. 5(a)–5(e). Pairs of dislocations with antiparallel Burger's vectors preserve both rotational and translational order. Shown in Fig. 5(a) is a virtual pair, also called a lattice shear or a twisted bond.[37] A virtual pair has no missing or additional bubbles. This dislocation pair arises by a slight distortion of a defect-free hexagonal lattice, and the two dislocations can annihilate in the same manner in which they were created. Virtual pairs can be thermally excited in bubble arrays at all densities, and are especially important close to the hexatic-to-liquid transition.[28,29] An interstitial and a vacancy are shown in Figs. 5(b) and 5(c), respectively. The glide plane of these dislocations are separated by one lattice spacing in the climb direction such that the extra rows add to give the vacancy or subtract to give an interstitial. Equivalently, this can be seen by drawing a Burger's circuit around the pair, counting the number of bubbles enclosed, and comparing this number with that for a perfect lattice.

The most common mode of dislocation interaction we observe is the glide of dislocations onto one another, resulting in combination into fewer dislocations or separation into more dislocations. As examples we have included two other observed structures in Figs. 5(d) and 5(e). These are three- and four-dislocation clusters corresponding to interstitials. The structure in Fig. 5(d) has been called a centered interstitial previously.[37] The structure in Fig. 5(b) can be recovered from the structure in Fig. 5(d) by gliding two dislocations onto one another and combining them. Similarly the structure in 5(d) can be recovered from that in 5(e) by dislocation glide. Gliding the two dislocation sin Fig. 5(b) onto each other gives a seven-four-seven triplet of disclinations, and this configuration is called an edge interstitial.[37]

V. QUASITHERMAL MOTION OF BUBBLES

Thermal motion of bubbles in our experiments is simulated by the application of an ac magnetic field H_{ac} superimposed on the dc field H_B. This ac field agitates the bubbles and produces random motion which simulates thermal Brownian motion corresponding to an effective temperature. This technique is standard in bubble memory technology to overcome the effects of coercive friction associated with microscopic roughness and allow bubbles to move freely. On the basis of observations and measurements we have constructed the following model for this phenomena.

In an ideal garnet film grown on a perfectly smooth substrate, an ac magnetic field acting on an isolated bubble with radius r in a dc bias field H_B produces a breathing motion of the bubble in which the bubble radius r undergoes a slight periodic contraction and expansion. Our observations indicate that the change in radius is small in our experiments, consistent with measurements indicating r does not vary appreciably with H_B.

Substrate roughness in otherwise ideal garnet films produces microscopic, random disorder on short-length scales. Because of this random disorder an isolated bubble in the applied ac field executes its breathing motion

on a rough surface analogous to sandpaper. When the bubble contracts and expands, this random potential produces a force on the bubble which changes its position slightly. As described below, we find that isolated bubbles diffuse in an apparently random way, indicating that the length scale of the random substrate potential is less than the size of the bubbles; we find no evidence of coherent motion.

Now consider an array of bubbles. Because the disorder is random and short range, the force on bubbles at different positions in the film is different. Therefore bubbles undergoing the same contraction and expansion cycles under the ac field at different positions are kicked in different directions, simulating thermal motion. We do not see any evidence for coherent motion of bubble arrays in the ac field, or the production of spatial patterns, indicating that the substrate potential is flat on length scales larger than the bubble radius. In substrates of lesser quality, not used in these experiments, we clearly observe patterning as bubbles are attracted to low spots in the substrate potential. The observed long-range uniformity of this microscopic frictional pinning for dilute bubble arrays indicates that the microscopic disorder has negligible structure at long wavelengths.

The random motion of isolated bubbles in garnet films is analogous to thermal Brownian motion. The motion of a bubble in the film can be described by a Langevin equation for the bubble velocity $v(t)$:

$$M dv(t)/dt + v(t)/B = F(t) + \not{F}(t) \ . \tag{3}$$

The term $v(t)/B$ represents the viscous drag experienced by the bubble as a result of many collisions with random substrate roughness; $F(t)$ is the net external force on a bubble and $\not{F}(t)$ is the rapidly fluctuating force which averages to zero over times much larger than the length of one ac cycle. In the absence of an external force $F(t)=0$, the bubble executes a random walk. The diffusion constant for bubble motion D is determined by the width of the Gaussian distribution of displacements from the initial position. For a constant external force F the bubble drifts with constant average velocity $\langle v(t) \rangle = BF$, where B is the bubble mobility. Assuming that the bubble motion is Brownian, an Einstein relation relates the mobility B to the diffusion constant D:

$$k_B T_{\text{eff}} = D/B \ . \tag{4}$$

Here, T_{eff} is the effective temperature of the bubble motion and k_B is Boltzman's constant. Thus the action of the ac field coupled with microscopic substrate roughness is to produce viscous Brownian motion of bubbles with an effective temperature T_{eff}. Note that all our experiments are performed at room temperature and we do not vary the *physical* temperature of the sample.

In order to characterize bubble jitter in an applied ac magnetic field and to study the effects of substrate roughness, we made detailed observations of the dynamics of the bubble motion. In these experiments the density of the bubble lattice was reduced to $\rho \sim 50\ \text{mm}^{-2}$ in order to minimize interactions between bubbles (regime 4). The dc bias H_B was held at 92 Oe for which the measured bubble radius is $r = 4.8\ \mu\text{m}$. An ac field of frequency 40 Hz and adjustable amplitude H_{ac} was applied. We then measured the diffusion constant D and the mobility B for the motion of isolated bubbles as described below. The time scales for all measurements were much larger than the time scale of the ac field ($\frac{1}{40}$ s).

The bubble diffusion constant D was measured by direct observations of the motion of individual bubbles in time under the influence of the ac field for a range of amplitudes H_{ac}. In order to do this we recorded the bubble motion for long periods of time and digitized images at periodic intervals for which the displacements were smaller than the bubble spacing. We followed the motion of each bubble from one image to the next by searching locally to find the nearest bubble. This algorithm accurately and quickly traces the path of each bubble in time. The paths of many bubbles were measured to statistically determine the diffusion constants D for isolated bubbles as a function of the ac field amplitude H_{ac}.

The mobility B of isolated bubbles was measured via the velocity of bubbles under the influence of an in-plane force applied by a magnetic field gradient. Consider an isolated bubble, with radius r in a dc bias field H_B applied along the z direction perpendicular to the film. A small gradient in the perpendicular magnetic field $\nabla H_Z(x)$ is applied by linearly varying the perpendicular field along the x direction, so that the direction of the gradient lies in the plane of the film. This gradient field produces an in-plane force on the bubble $-\mu \nabla H_Z(x)$. In our experiments the gradient field was produced by a pair of opposing coils on either side of the sample. The collapse field of isolated bubbles was used to measure and characterize the gradient magnetic field; the field is linear to $\pm 3\%$ over a 3000-μm region of the sample for a 0.011 Oe/μm gradient.

The bubble mobility B was measured by subjecting bubbles to a constant in-plane external force F via a gradient magnetic field. The magnitude of the applied field gradient was 0.005 Oe/μm for which $F = 8 \times 10^{-7}$ dynes. For this field gradient the bubble radius does not change appreciably over 3000 μm, much larger than the field of view. The bubble motion produced by this in-plane force was recorded as above, and the bubble drift velocities v parallel to F were directly measured for different values of H_{ac} and used to determine the mobility $B = v/F$.

The measured bubble diffusion constant D and mobility B are plotted versus the amplitude of the ac field H_{ac} in Figs. 6(a) and 6(b). As shown, the diffusion constant D rises rapidly with H_{ac}, whereas the mobility B increases linearly with H_{ac} above a depinning threshold. The effective temperature T_{eff} of the bubbles was measured using Einstein's relation Eq. (4) and is shown versus H_{ac} in Fig. 7; the dashed line in Fig. 7 is a linear fit to the data. As shown by this data, the ac magnetic field coupled with microscopic substrate roughness simulates thermal motion with effective temperatures $T_{\text{eff}} \sim 10^5$ K. Figure 7 indicates that the analogy between quasithermal motion of isolated magnetic bubbles and the Brownian motion of pollen grains is good, but not perfect: there might be small deviations from ideal Brownian dynamics in the motion of magnetic bubbles.

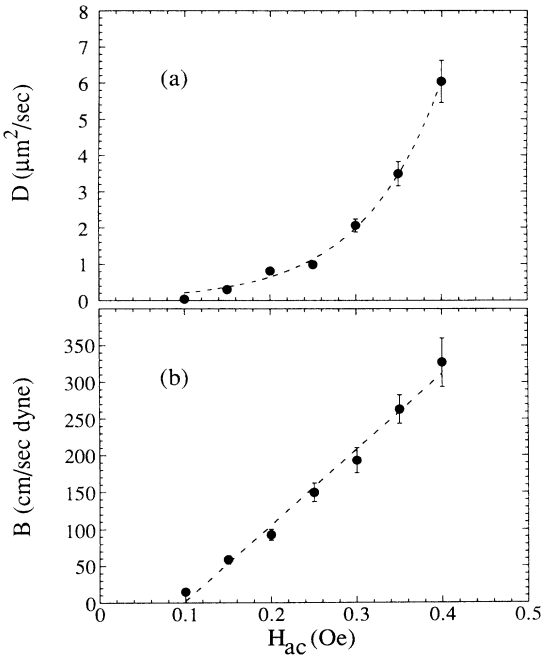

FIG. 6. (a) Measured bubble diffusion constant D vs peak-to-peak amplitude of the applied ac field H_{ac} at frequency 40 Hz, for isolated bubbles (density $\rho = 50$ mm^{-2}). The dashed line is an exponential fit to the data. (b) Measured bubble mobility B vs peak-to-peak amplitude of the applied ac field H_{ac}, for the same conditions as in (a). The dashed line is a linear fit to the data.

As shown by the Arrhenius plot of the measured diffusion constant D versus inverse temperature $1/T_{eff}$ in Fig. 8, the diffusion of isolated bubbles is activated. The diffusion constant for a simple hopping model is $D = \nu L_P^2 \exp(-E_P/k_B T)$, where the attempt rate ν is equal to the driving frequency 40 Hz, the average length per hop is the pinning length scale L_P, and the Boltzman factor is the probability of success for hopping over a pinning energy barrier E_P. From the fitted dashed line in Fig. 8 we obtain estimates of the pinning length scale $L_P \cong 0.4$ μm and the pinning energy $E_P \cong 1 \times 10^6$ K, which are consistent with the discussion of diffusive bubble motion given above. Because L_P is much smaller than the bubble radius, we are justified in assuming that the length scale of the substrate roughness is short. Also, the pinning energy is larger than the measured effective temperatures, consistent with a simple model for activated diffusion.

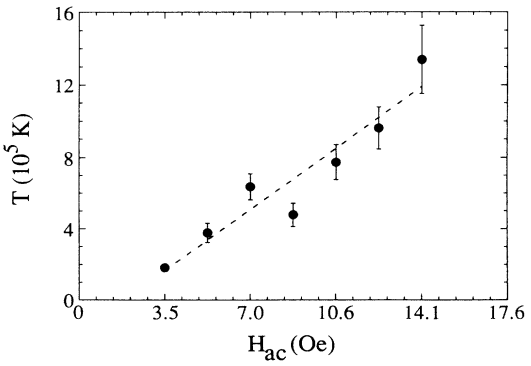

FIG. 7. Measured effective bubble temperature T_{eff} vs peak-to-peak amplitude of the applied ac field H_{ac}, determined from measured diffusion constant D and mobility B via Einstein's relation (see text). The dashed line is a linear fit.

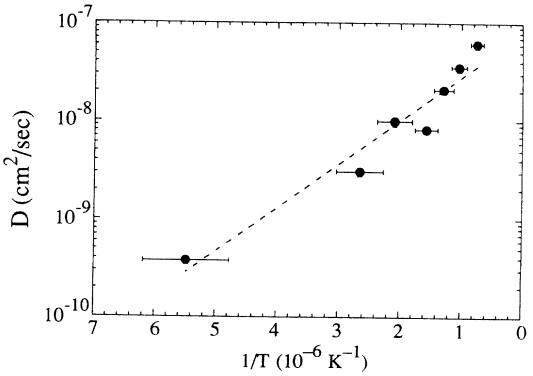

FIG. 8. Arrhenius plot of the measured bubble diffusion constant D vs effective temperature T_{eff}. The dashed line is a fit of the form: $D = \nu L_P^2 \exp(-E_P/k_B T)$ (see text).

The absence of coherent motion of isolated bubbles, and the fact that they show no observable tendency to bunch together or form patterns, is strong evidence that the garnet films used in this work are free from significant inhomogeneity on long length scales that are comparable to and larger than a bubble radius. The garnet film used for this work is a single crystal grown on an untwinned single crystal substrate. In the presence of an agitating ac field, isolated bubbles are free to move. If minima in the total potential were present the bubbles would flow toward them, thus decorating large-scale inhomogeneities in film thickness or magnetic properties. In fact we have seen bunching and pattering of this type in lesser-quality garnet films, not used in this experiment.

VI. SUMMARY

In this paper we have described the structural and thermal properties of magnetic-bubble arrays in thin garnet films. Structural defects in the bubble arrays are visualized and expressed in terms of simple disclinations and dislocations. Dislocation pairs are observed which correspond to virtual pairs, and lattice vacancies and interstitials. Dislocations are found to interact primarily via glide, although climb is observed. Dislocation and disclination motion is made possible in these arrays by ac-field induced bubble jitter. Microscopic substrate roughness couples with periodic forcing to produce diffusive bubble motion. The effective temperature and diffusion constant for bubble motion are measured versus the amplitude of the ac field, and it is found that diffusion is thermally activated. These measurements also indicate that the microscopic random substrate potential has length scale less than the bubble size and energy greater than the effective temperature. These properties of magnetic-bubble arrays make this system well suited to studies of the melting transition in two dimensions.

ACKNOWLEDGMENTS

It is a pleasure to thank David Nelson for very helpful, insightful, and encouraging comments and suggestions. We thank Roger Belt and the Airtron Division of Litton Industries for the garnet films and Ken Babcock for helpful conversations. This work was supported by the Office of Naval Research under Grants Nos. N00014-89-J-1592 and N00014-89-J-1023.

[1]D. R. Nelson, in *Phase Transitions and Critical Phenomena,* edited by C. Domb and J. L. Lebowitz (Academic, London, 1983), Vol. 7.

[2]K. J. Standburg, Rev. Mod. Phys. **60**, 161 (1988).

[3]*Ordering in Two Dimensions,* edited by S. K. Sinha (North-Holland, Amsterdam, 1980).

[4]D. R. Nelson, M. Rubinstein, and F. Spaepen, Philos. Mag. A **46**, 105 (1982).

[5]C. A. Murray and D. H. Van Winkle, Phys. Rev. Lett. **58**, 1200 (1987).

[6]C. A. Murray and R. A. Wenk, Phys. Rev. Lett. **62**, 1643 (1989).

[7]C. A. Murray, W. O. Sprenger, and R. A. Wenk, Phys. Rev. B **42**, 688 (1990).

[8]Y. Yang, A. J. Armstrong, R. C. Mockler, and W. J. O'Sullivan, Phys. Rev. Lett. **62**, 2401 (1989).

[9]G. Helgesen and A. T. Skjeltorp, Physica A **170**, 488 (1991).

[10]C. A. Murray, P. L. Gammel, D. J. Bishop, D. B. Mitzi, and A. Kapitulnik, Phys. Rev. Lett. **64**, 2312 (1990).

[11]D. G. Grier, C. A. Murray, C. A. Bolle, P. L. Gammel, D. J. Bishop, D. B. Mitzi, and A. Kapitulnik, Phys. Rev. Lett. **66**, 2270 (1991).

[12]A. H. Eschenfelder, *Magnetic Bubble Technology* (Springer-Verlag, New York, 1981).

[13]A. P. Malozemoff and J. C. Slonczweski, *Magnetic Domain Walls in Bubble Materials* (Academic, New York, 1979).

[14]T. H. O'Dell, Rep. Prog. Phys. **49**, 589 (1986).

[15]C. Kooy and U. Enz, Phillips Res. Rep. **15**, 7 (1960).

[16]A. H. Bobeck, Bell Sys. Tech. J. **46**, 1901 (1967).

[17]A. A. Thiele, Bell Sys. Tech. J. **48**, 3287 (1969).

[18]A. A. Thiele, J. Appl. Phys. **41**, 1139 (1970).

[19]A. A. Thiele, A. H. Bobeck, E. Della Torre, and U. F. Gianola, Bell Sys. Tech. J. **50**, 711 (1971).

[20]A. A. Thiele, Bell Sys. Tech. J. **50**, 725 (1971).

[21]K. L. Babcock and R. M. Westervelt, Phys. Rev. Lett. **63**, 175 (1989).

[22]K. L. Babcock and R. M. Westervelt, Phys. Rev. A **40**, 2022 (1989).

[23]K. L. Babcock, R. Seshadri, and R. M. Westervelt, Phys. Rev. A **41**, 1952 (1990).

[24]K. L. Babcock and R. M. Westervelt, Phys. Rev. Lett. **64**, 2168 (1990).

[25]K. L. Babcock, Ph.D. thesis, Harvard University, 1989, available from United Microfilms International, Ann Arbor, MI.

[26]M. Seual and R. Wolfe, Phys. Rev. Lett. **68**, 2460 (1992).

[27]M. Seul, L. R. Monar, L. O'Gorman, and R. Wolfe (unpublished).

[28]R. Seshadri and R. M. Westervelt, Phys. Rev. Lett. **66**, 2774 (1991).

[29]R. Seshadri and R. M. Westervelt, following paper, Phys. Rev. B **46**, 5150 (1992).

[30]R. F. Belt and J. B. Ings, SPIE J. **753**, 142 (1987).

[31]C. Kittel, Rev. Mod. Phys. **21**, 541 (1949).

[32]J. A. Cape and G. W. Lehman, J. Appl. Phys. **42**, 4732 (1971).

[33]G. R. Woolhouse and P. Chaudhari, Philos. Mag. **31**, 161 (1974).

[34]F. P. Preparata and M. I. Shamos, *Computational Geometry, An Introduction* (Springer-Verlag, New York, 1985).

[35]F. R. N. Nabarro, *Theory of Crystal Dislocations* (Dover, New York, 1987).

[36]J. Friedel, *Dislocations* (Pergamon, London, 1964).

[37]Daniel S. Fisher, B. I. Halperin, and R. Morf, Phys. Rev. B **20**, 4692 (1979).